

# Temporal Evolution of Erosion in Pore-Networks: From Homogenization to Instability

Ahmad Zareei, Deng Pan, and Ariel Amir\*

*School of Engineering and Applied Sciences, Harvard University, Cambridge, MA, 02148*

(Dated: December 22, 2021)

## S1. SIMULATION ALGORITHM

In our simulations, we tested two types of networks: (i) a topologically ordered (diamond-grid) network, (ii) a topologically random network (2d and 3d). The 2d random network is created using uniformly distributed points with on average  $N_x \times N_y$  nodes in the horizontal and vertical directions where the randomly distributed points are connected using a Delaunay triangulation. The 3d random network similarly is obtained by a uniform distribution of  $N_x \times N_y \times N_z$  points in space, where the the points are connected using Voronoi cell initialization. The diameter of each edge is sampled from either a uniform distribution with  $\mathcal{U}(1, 14)$ , log-normal distribution with  $\mu = 3, \sigma = 0.48$ , or truncated normal distribution with  $\mathcal{N}(\mu = 7.0, \sigma = 3.6)$ , where all of the distributions have a coefficient of variation close to 0.5. An external pressure is considered between the left-most nodes and the rightmost nodes ( $p_{\text{left}} = 10, p_{\text{right}} = 0$ ). For each edge, assuming a Poiseuille flow, the fluid flux  $q$  and pressure difference  $\delta P_e$  are related through  $q_e = C_e \delta P_e$ , where  $C_e = \pi r_e^4 / 8\mu L_e$ ,  $L_e$  is the length of the tube, and  $\mu$  is the viscosity of the fluid. We define  $\vec{q}_e$  as the vector of fluid flux through all the edges, and as a result  $\vec{q}_e = \mathbf{CD}\vec{P}_n$  where  $\vec{P}_n$  is the vector of pressure at all the nodes,  $\mathbf{D}$  is the transpose of the network's oriented incidence matrix, and  $\mathbf{C}$  is the diagonal matrix of edge conductances  $\mathbf{C}_e = \text{diag}(C_e^{(1)}, C_e^{(2)}, \dots, C_e^{(N_e)})$ . The orientation (or direction) of an edge is arbitrary selected, and it only determines the positive direction for the fluid flow in that edge. Next, we use conservation of mass at the nodes to solve for the network pressure/flux at the nodes/edges. The conservation of mass at each node is

$$\vec{q}_n = \mathbf{D}^\top \mathbf{CD}\vec{P}_n, \quad (\text{S1})$$

where  $\vec{q}_n$  is the vector of total incoming flow to each node. The total incoming flow to an internal node is zero inside the network due to the conservation of mass, and can only be non-zero at the boundary nodes. Without loss of generality, we renumber the boundary nodes to  $1, 2, \dots, N_B$ , where  $N_B$  shows the total number of nodes at the boundary. We re-partition Eq. (S1) to obtain

$$\begin{bmatrix} \mathbf{D}_b^\top \mathbf{CD}_b & \mathbf{D}_b^\top \mathbf{CD}_n \\ \mathbf{D}_n^\top \mathbf{CD}_b & \mathbf{D}_n^\top \mathbf{CD}_n \end{bmatrix} \begin{bmatrix} P_1^{BC} \\ P_2^{BC} \\ \vdots \\ P_{N_B}^{BC} \\ \hline P_{N_B+1} \\ \vdots \\ P_{N_n} \end{bmatrix} = \begin{bmatrix} q_1^{BC} \\ q_2^{BC} \\ \vdots \\ q_{N_B}^{BC} \\ \hline 0 \\ \vdots \\ 0 \end{bmatrix} \rightarrow \begin{bmatrix} \mathbf{A}_{bb} & \mathbf{A}_{bn} \\ \mathbf{A}_{nb} & \mathbf{A}_{nn} \end{bmatrix} \begin{bmatrix} P_1^{BC} \\ P_2^{BC} \\ \vdots \\ P_{N_B}^{BC} \\ \hline P_{N_B+1} \\ \vdots \\ P_{N_n} \end{bmatrix} = \begin{bmatrix} q_1^{BC} \\ q_2^{BC} \\ \vdots \\ q_{N_B}^{BC} \\ \hline 0 \\ \vdots \\ 0 \end{bmatrix}, \quad (\text{S2})$$

where  $\mathbf{A}_{st} = \mathbf{D}_s^\top \mathbf{CD}_t^\top$  and  $s, t \in \{a, b\}$ . The first  $N_B$  elements of the pressure vector (i.e.,  $P_1, \dots, P_{N_B}$ ) represent the pressure at the boundary nodes and the rest represent the pressure for the internal nodes. In summary the above equations can be written as a combination of two set of linear equations

$$\mathbf{A}_{bb}\vec{P}_{BC} + \mathbf{A}_{bn}\vec{P} = \vec{q}_{BC}, \quad (\text{S3a})$$

$$\mathbf{A}_{nb}\vec{P}_{BC} + \mathbf{A}_{nn}\vec{P} = 0. \quad (\text{S3b})$$

where  $\vec{P}_{BC} = [P_1^{BC}, \dots, P_{N_B}^{BC}]^\top$  is the boundary nodes pressure vector,  $\vec{q}_{BC} = [q_1^{BC}, \dots, q_{N_B}^{BC}]^\top$  is the boundary nodes incoming fluid flux vector, and  $\vec{P} = [P_{N_B+1}, \dots, P_{N_n}]^\top$  is the unknown pressure vector for the rest of the nodes. If

---

\* arielamir@seas.harvard.edu

the pressure at the boundary is given, we can use Eq. (S3b) to solve for the internal pressure values  $\vec{P}$ , and then use Eq. (S3a) to find the required flux at the boundary nodes  $\vec{q}_{BC}$ . However, if fluid flux vector at the boundary nodes is given (i.e.,  $\vec{q}_{BC}$  is known), we need to simultaneously solve Eqs. (S3a) and (S3b) to find the boundary pressure vector  $\vec{P}_{BC}$  and internal nodes pressure vector  $\vec{P}$ . In either case, solving Eq. (S3) results in the nodes' pressure vector and also the fluid flux vector at the boundary nodes. The fluid flux at each edge can then be calculated using  $\vec{q}_e = \mathbf{C}_e \mathbf{D} \vec{P}_n$ . Next, given the flux at each edge  $q_e$ , we increase (decrease) the edge radius under erosion (clogging) using

$$\frac{dr_e}{dt} \propto \pm \frac{q_e^m}{r_e^n}, \quad (\text{S4})$$

and re-iterate the process to solve for the new fluid flux vector. We use a simple forward Euler for time integration. For each iteration, we choose the time step  $dt$  so that  $\max(dr_e) = 0.1r_0$ , where  $r_0$  is the smallest radius among all edges. This condition guarantees that at each step a small amount of material is eroded and there is no sudden change in the network. We further test the convergence by decreasing  $\max(\Delta r_{ij})$  to half and we observe that the average relative change in the flux vector is  $\approx 1.2\%$ , and the PDFs remain intact without any notable change. The network size for the 2d/3d networks is  $N_x = 100, N_y = 50/N_x = 50, N_y = 12, N_z = 12$  unless mentioned otherwise. In either case, the network has an order of  $10^3$  edges. Note that the physical assumption of low Reynolds regime  $\text{Re} \ll 1$  at all times ensures that the Poisoule flow assumption remains valid. Additional dimensionless transport numbers such as the Péclet number (ratio of advection to diffusion) or the Damkohler number (ratio of chemical reaction rate to the transport phenomena rate) are assumed to be respectively very large and very small, resulting in advection to be much stronger than diffusion and chemical reaction. It is to be noted that considering diffusion or chemical reactions might change the dynamics of erosion as it requires tracking a secondary concentration field that might affect the local erosion law. The code is publicly available in a GitHub repository [1].

## S2. ANALYTICAL RESULTS FOR FLUID FLUX EXP-TAIL PDF IN A DIAMOND NETWORK

As described in the main text, the PDF of flow in a topologically disordered network of tubes takes the same form as in a structured diamond grid. For completeness, here we repeat the derivation of Refs. [2–4] which show that the observed exponential distribution of fluid flux can be described using a mean-field approach on a structured grid. Basically, the random distribution of the diameters along with the conservation of mass in the network are the two main ingredients resulting in an exponential tail distribution. In a diamond grid, the incoming flow to a node is redistributed among the outgoing edges (since fluid mass is conserved). Due to the randomness in the tube's diameter, the redistribution of the incoming flow to a node between the outgoing edges is random variable. This model for the flow can be mapped one to one to the problem of force fluctuations in a bead pack [2–4] as shown in Fig. S1. In a bead pack, the force at each layer is redistributed to the next layer where the total force exerted on the next layer should equal to that of the previous layer. Given the above conditions, the flow at layer  $L + 1$  at node  $j$  can be

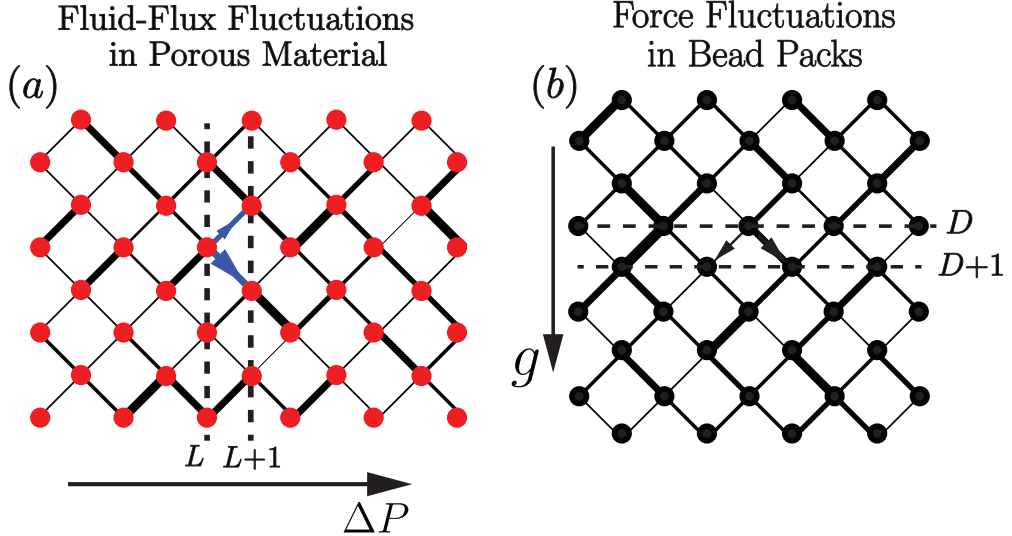


FIG. S1: (a) Schematic of a diamond grid network of tubes. The incoming flow to each node is redistributed among the outgoing edges. The thickness of the lines shows the fluid flux transferred through that edge. (b) Schematic diagram showing beads (represented with nodes) and their contacts to the neighboring sites (represented with edges). The thickness of the edges show the force transferred through that contact.

obtained as

$$q(L + 1, j) = \sum_i w_{ij} q(L, i) = w_{i,i+1} q(L, i + 1) + w_{i,i} q(L, i), \quad (\text{S5})$$

where  $w_{ij}$  shows the weights by which the flow is redistributed, and  $\sum_j w_{ij} = 1$  since the total fluid flux is conserved. Assuming a general distribution of for the weights,  $\eta(w)$ , we can use a mean-field approximation to find the distribution of  $q$  at the layer  $L$ , i.e.,  $p_L(q)$ , as

$$p_L(q) = \prod_{j=1}^N \left\{ \int_0^1 dw_j \eta(w_j) \int_0^\infty dq_j p_{L-1}(q_j) \right\} \times \delta \left( \sum_j w_j q_j - q \right), \quad (\text{S6})$$

where  $N$  is the number of outgoing edges (e.g., in our structured diamond grid  $N = 2$ ) and  $\delta(\cdot)$  is the Dirac delta function. Taking the Laplace transform of the above equation and defining  $\tilde{p}(s) \equiv \int_0^\infty p(q) e^{-qs} dq$  one obtains

$$\tilde{P}_L(s) = \left( \int_0^1 dw \eta(w) \tilde{P}_{L-1}(sw) \right)^N. \quad (\text{S7})$$

The above equation gives a recursive relation for the Laplace transformed of fluid flux PDF,  $\tilde{P}_L(s)$ , where it gradually converges to a distribution  $\tilde{P}(s)$  from which the PDF of fluid flux can be obtained. Solving the above equation for a structured diamond grid network, one finds that the converged PDF of the fluid flux becomes  $p(q) = 4q \exp(-2q)$  [2–4], which is an exponential tailed distribution.

### S3. ROBUSTNESS TO TOPOLOGY, INITIAL CONDITION, AND BOUNDARY CONDITION

In order to check the robustness of our results with respect to the topology of the network, we run our simulations on a three-dimensional random network with Voronoi cell initialization of nodes in space (Fig. S2), and also for a two dimensional topologically ordered network with a diamond grid (Fig. S3), where both networks are initialized with a uniform random distribution for the diameter of the tubes. We find that regardless of the topology of the network, an erosion dynamics with  $n > 3$  results in a homogenized network, while  $n < 3$  results in the channelization instability. We further check the effect of initial randomness on the fate of the network. We use a two-dimensional diamond-grid network with a narrow uniform initial distribution of tube diameters around an average diameter  $d_0$  with only a very small variation (3%), i.e., the tube diameters are sampled from a uniform distribution with  $\mathcal{U}(d_0(1 - \epsilon), d_0(1 + \epsilon))$ . We again find that for the networks with  $n < 3$  channels are formed, while for  $n > 3$  the network stays homogenized. In addition to the network topology and initial condition, we test the robustness of our results to changes in the boundary condition. We choose a circular domain, with the central node being the inlet and all the nodes at the outer boundary being outlets. Similar to the transition reported for the square domain, we find a phase transition at the predicted power which shows that our analysis is independent of the geometry (Fig. S5).

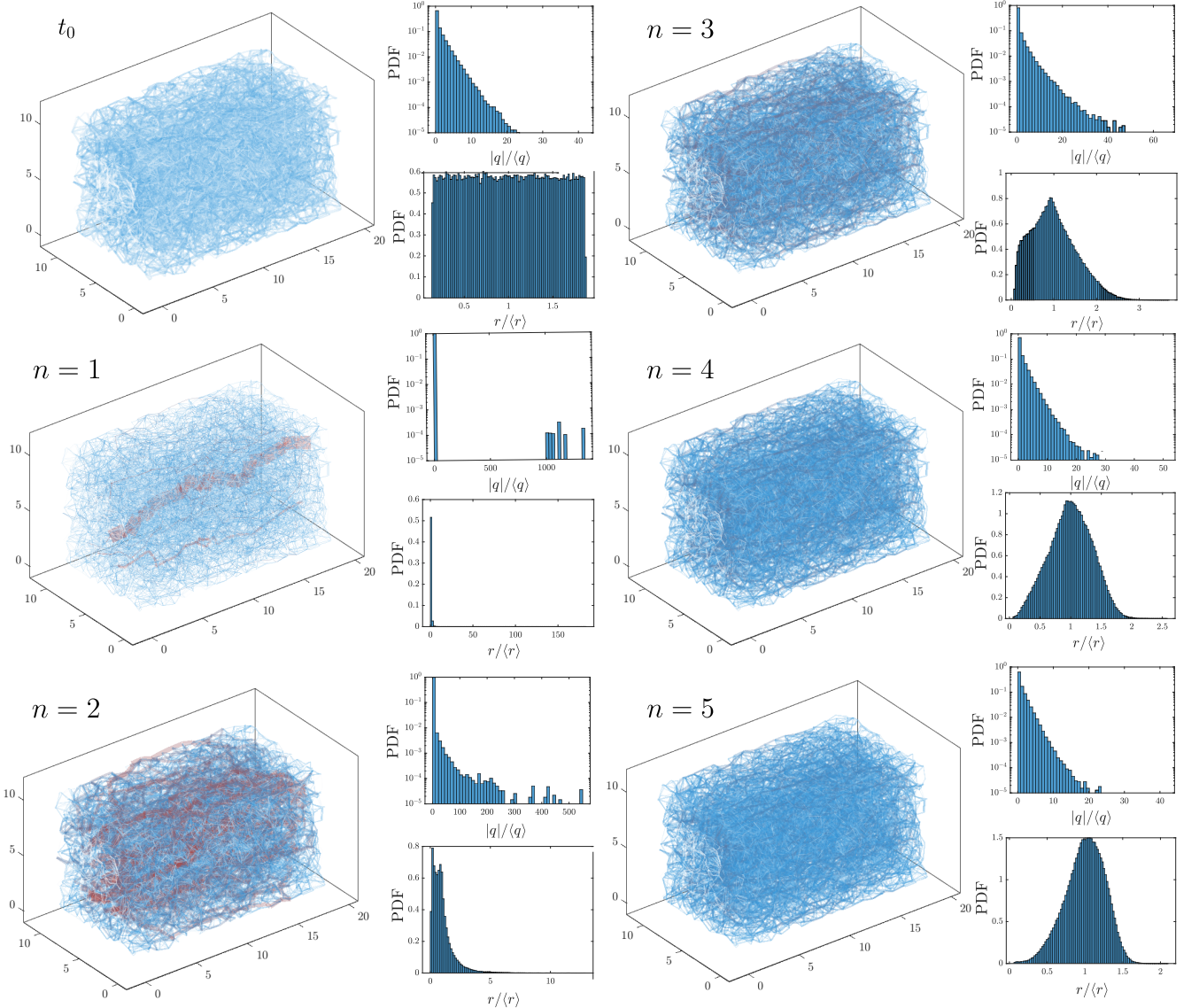


FIG. S2: Erosion in a topologically random 3D network of tubes with  $N_x = 20, N_y = 12, N_z = 12$  points for Voronoi cell initialization and an initial uniform broad distribution of tube diameters randomly sampled from a uniform distribution with  $\mathcal{U}(1, 14)$ . Snapshots of the network, PDF of normalized fluid flux  $q/\langle q \rangle$ , and normalized edge radius distribution  $r/\langle r \rangle$  at the initial time  $t = 0$ , and also after  $N$  erosion steps for different powers of erosion  $n$  are shown. We stop the erosion after  $N$  steps such that  $\langle r \rangle = 2r_0$  where  $r_0 = \langle r_{t=0} \rangle$ . The erosion law is based on  $dr/dt = \alpha q/r^n$  where different powers of  $n$  correspond to different models of erosion.

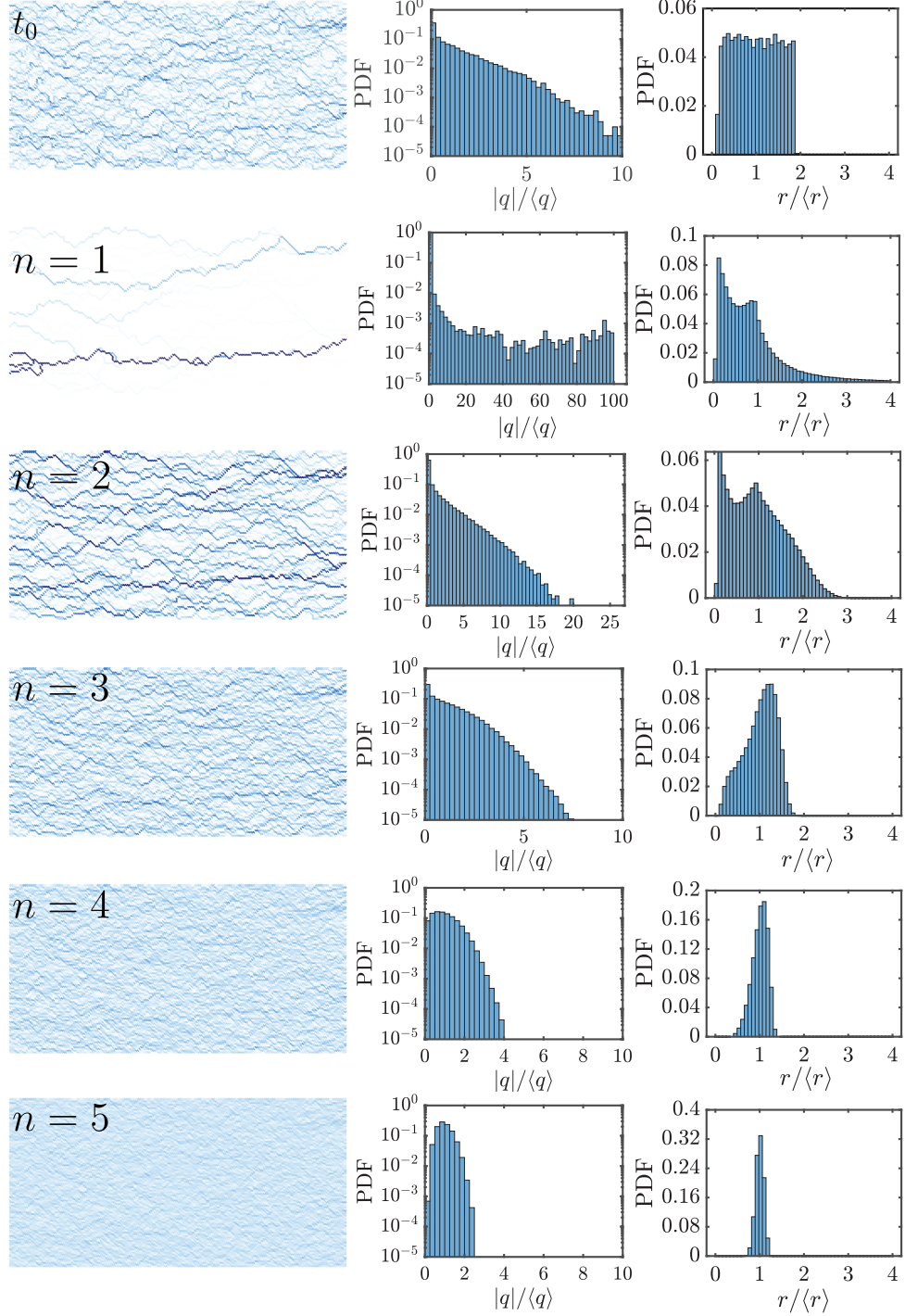


FIG. S3: Erosion in a diamond grid network with  $N_x = 100$ ,  $N_y = 50$  randomly distributed nodes and an initially broad distribution of tube diameter randomly sampled from a uniform distribution with  $\mathcal{U}(1, 14)$ . The initial condition is shown with the label  $t = 0$  in the first row. Each row afterward corresponds to the simulation result after  $N$  steps such that  $\langle r \rangle = 2r_0$  where  $r_0 = \langle r_{t=0} \rangle$  or twice the initial average radius. The erosion law is based on Eq. (1) in the main text where different powers of  $n$  correspond to different models of erosion. The first column is a snapshot of the pore network, the second column is the PDF of normalized fluid flux  $q/\langle q \rangle$ , and the last column is the PDF of normalized radius  $r/\langle r \rangle$ .

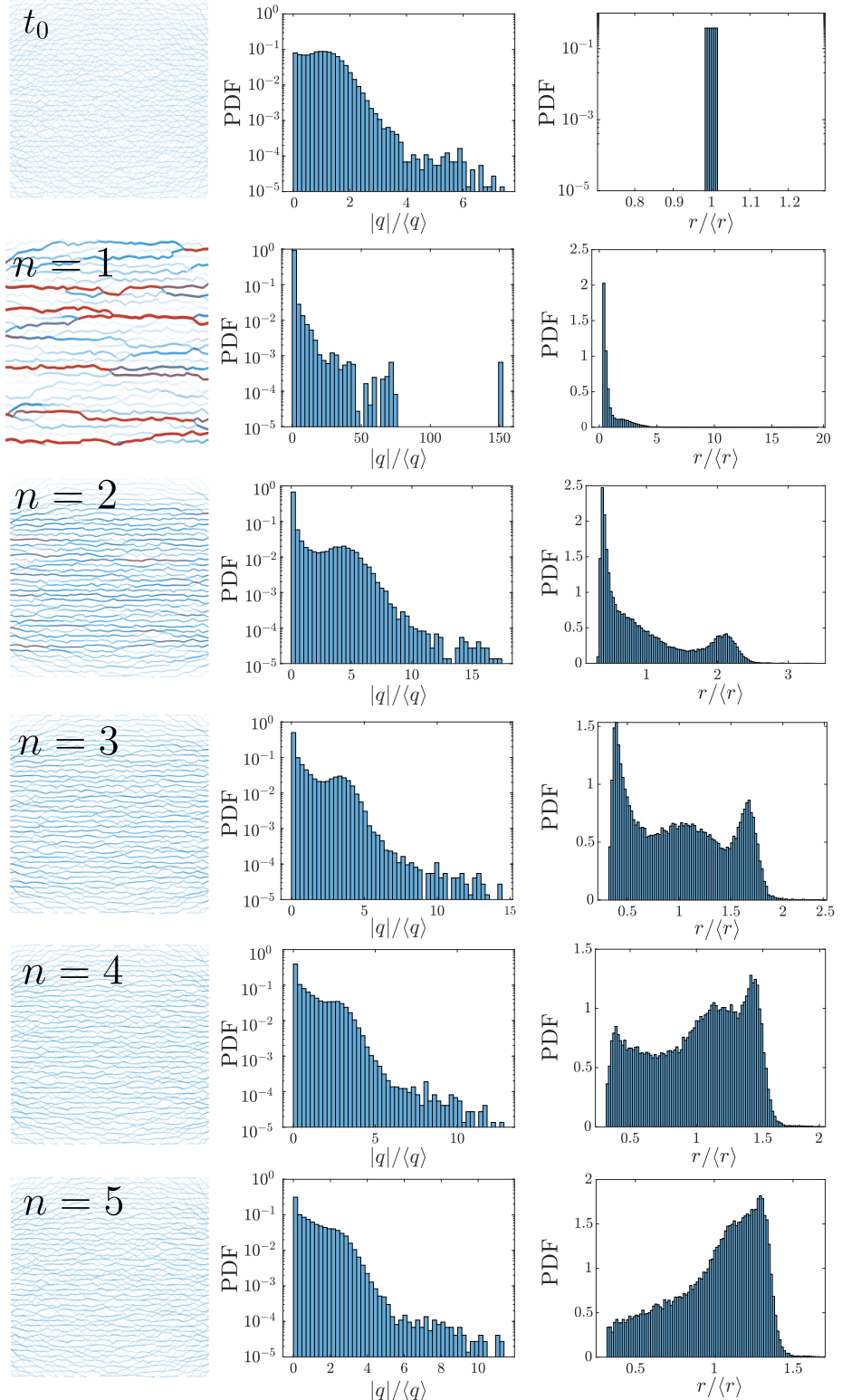


FIG. S4: Erosion in a structured diamond grid network with  $N_x = 50$ ,  $N_y = 50$  and an initially narrow distribution of tube diameters randomly sampled from a uniform distribution with  $\mathcal{U}(d_0(1 - \epsilon), d_u(1 + \epsilon))$  where  $d_0$  is the average diameter and  $\epsilon = 0.03$ . The initial condition is shown with the label  $t = 0$  in the first row. Each row afterward corresponds to the simulation result after  $N$  steps such that  $\langle r_{t=N} \rangle = 2r_0$  where  $r_0 = \langle r_{t=0} \rangle$  or twice the initial average radius. The erosion law is based on Eq. (1) in the main text where different powers of  $n$  correspond to different models of erosion. The first column is a snapshot of the pore network, the second column is the PDF of normalized radius  $r/\langle r \rangle$ .

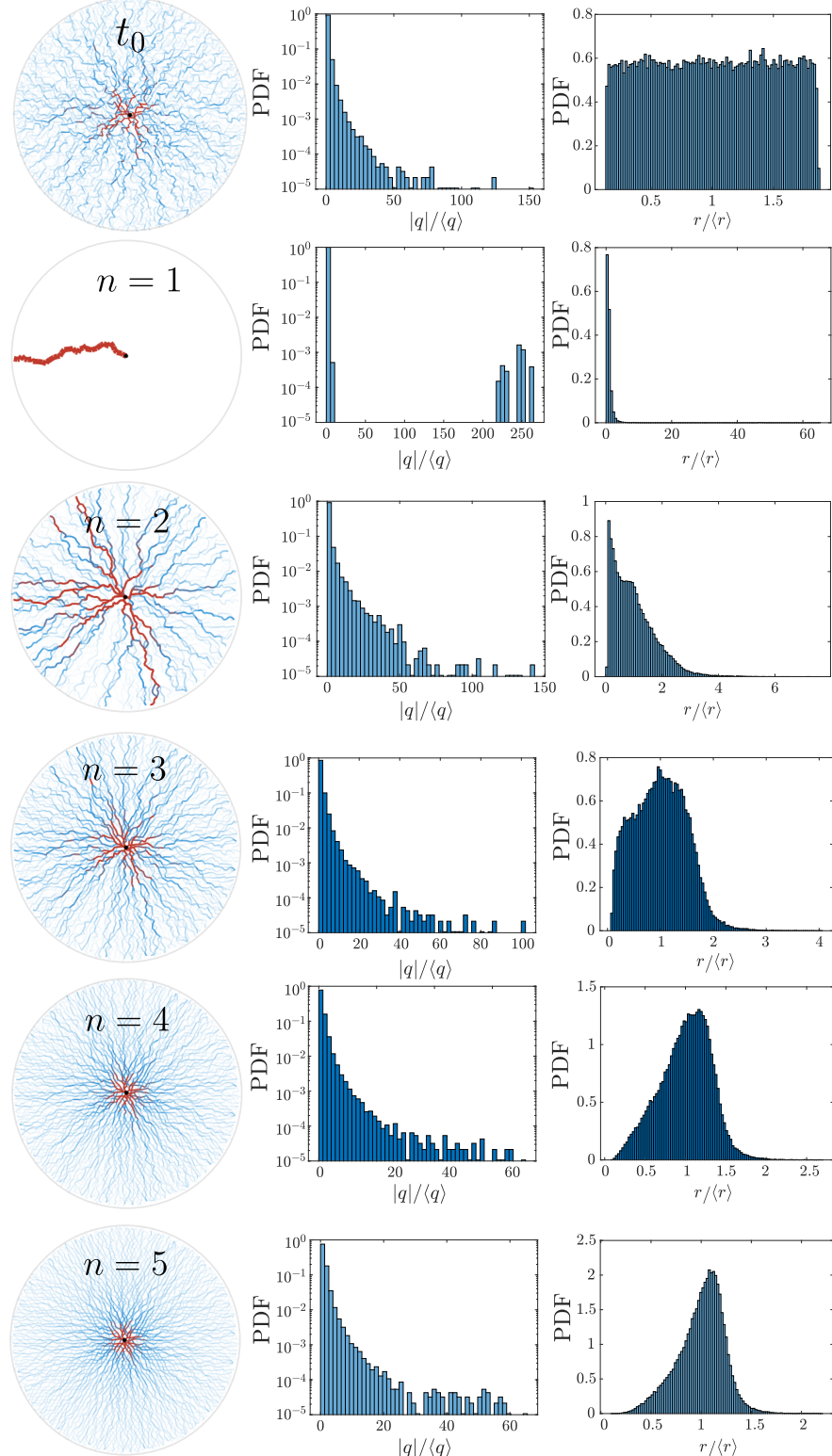


FIG. S5: Erosion in a topologically random 3D network of tubes with a circular topology with  $N = 3000$  randomly distributed nodes and an initial uniform broad distribution of tube diameters randomly sampled from a uniform distribution with  $\mathcal{U}(1, 14)$ . Shown are snapshots of the network, PDF of normalized fluid flux  $q/\langle q \rangle$ , and normalized edge radius distribution  $r/\langle r \rangle$  at the initial time  $t = 0$ , and also after  $N$  erosion steps for different powers of erosion  $n$ . We stop the erosion after  $N$  steps such that  $\langle r \rangle = 2r_0$  where  $r_0 = \langle r_{t=0} \rangle$ . The erosion law is based on Eq. (1) in the main text where different powers of  $n$  correspond to different models of erosion.

#### S4. EROSION WITH A THRESHOLD

In order to make our erosion model more realistic, we modify the model as

$$\frac{dr}{dt} = \begin{cases} q^m/r^n - \beta & q^m/r^n \geq \beta \\ 0 & q^m/r^n < \beta \end{cases} \quad (\text{S8})$$

where  $\beta$  is the threshold for the onset of erosion. We pick  $\beta = 0.25\langle q^m/r^n \rangle$  and  $\beta = 0.9\langle q^m/r^n \rangle$  corresponding to a small and a large threshold value. In both cases, we ran our simulations for different values of  $m$  and  $n$ , and found that different behaviors of homogenization and channelization persists (see Fig. S6). The result can be explained by applying the general condition for the phase transition as discussed in the main text. Following the same argument, it can be shown that the homogenization condition (Eq. 3 in the main text) is equivalent to the condition

$$4m - n - 1 < -\frac{\beta}{q^m/r^n}. \quad (\text{S9})$$

which can be found using  $g(r) = (\pi\Delta p/8\mu L)^m r^{m-n} - \beta$  assuming a constant pressure boundary condition. Note that the condition above depends on the value of  $q^m/r^n$  which varies over the network edges. Taking the mean value of  $q^m/r^n$  to find an average value for the transition condition, the transition line becomes  $4m - n = 0.75$  and  $4m - n = 0.1$  for the small and large thresholding value respectively. As a result the thresholding condition slightly shifts the intercept of the transition line while the slope remains the same. In Fig. S6, we plot the new transition lines, where the prediction for the phase boundaries matches well with the simulation results.

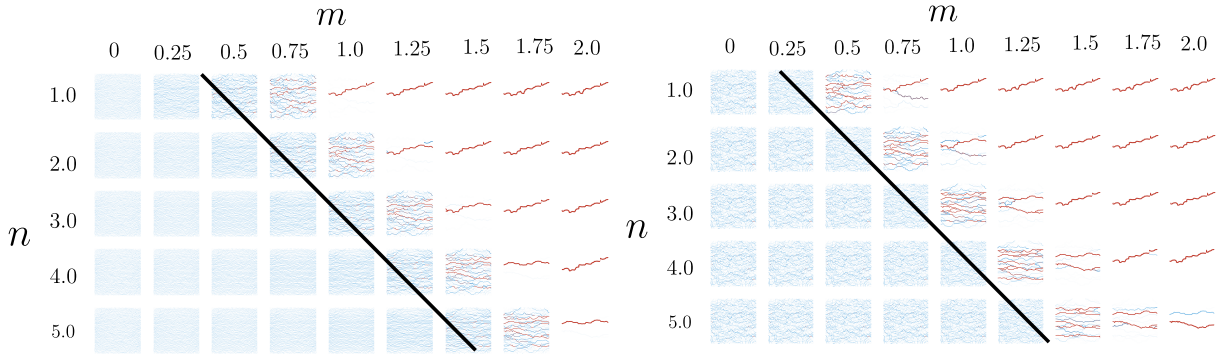


FIG. S6: Evolution of a randomly initialized network for various powers of  $m$  and  $n$  in Eq. (S8) with a small threshold value of  $\beta = 0.25\langle q^m/r^n \rangle$  (left figure), and a large threshold value of  $\beta = 0.9\langle q^m/r^n \rangle$  at  $t = 0$ . The network is randomly initialized with  $50 \times 50$  randomly distributed pores. The black line shows the theoretical transition boundary between channelization instability and homogenization obtained using local dynamics model, i.e.,  $4m - n = 0.75$  (left figure), and  $4m - n = 0.1$  (right figure).

## S5. AVERAGE CHANGE IN THE ORDER PARAMETER

In order to quantify the network behavior shown in Fig. 4, we calculate the change in the order parameter for different  $m, n$  averaged over 100 simulations with different random initial conditions, and the heat-map results are shown in Fig. S7. The positive or negative change in the order parameter shows the network's change toward homogenization or channelization. The boundary between the two phases (homogenization and channelization) calculated using the simple model introduced in the main text is shown with a solid black line here, and it can be seen that it agrees well with the order parameter change.

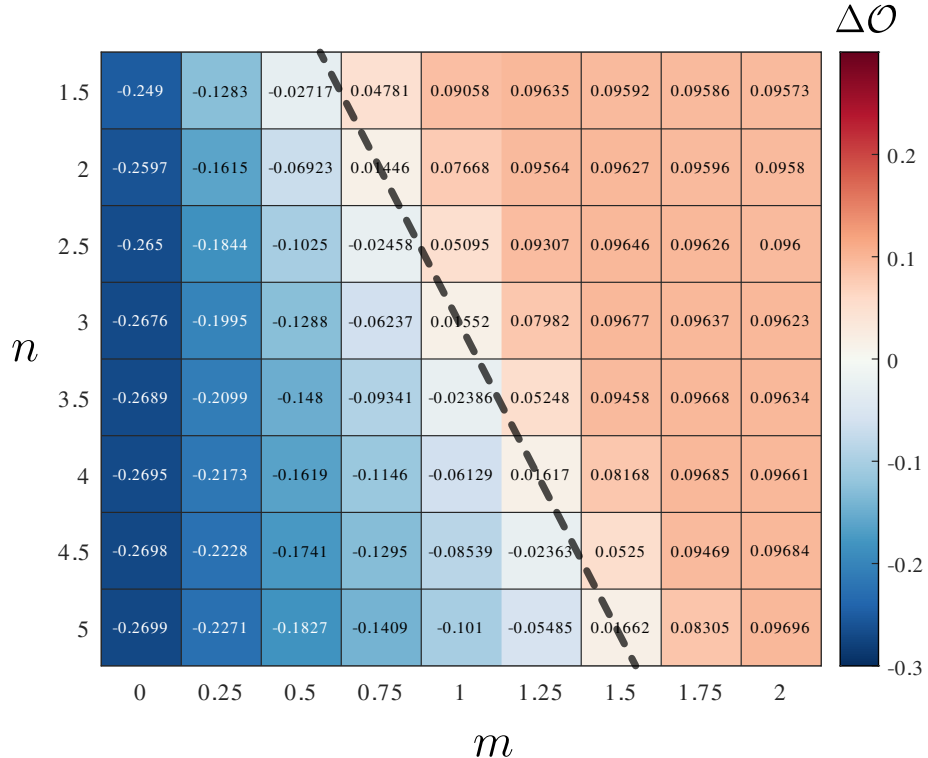


FIG. S7: The heat map for the average change in the order parameter corresponding to the networks shown in Fig. 4 of the main text. The order parameter shown in the heat map here is an average of 100 different simulations with different random initialization of tube diameters. The black line shows the boundary between two phases calculated using the model introduced in the main text.

## S6. CLOGGING DYNAMICS

Besides erosion, another change in the network is the deposition/sedimentation of material on the boundary walls of the porous material. We refer to this dynamical change a “clogging” process as opposed to erosion. Contrary to erosion, the clogging behavior may cause some edges to block which effectively alters the network of connectivity and network behavior. This change in the connection between nodes through edges getting blocked can drastically alter porous structure behavior, e.g., causes a huge difference between effective and true porosity [5]. Despite the drastic change of network with blockages, we can still focus on the *initial* change in the order parameter. The derivative of order parameter can be written as

$$\frac{d\mathcal{O}}{dt} = \sum_{ij} \sum_{kl} \frac{\partial\mathcal{O}}{\partial q_{ij}} \frac{\partial q_{ij}}{\partial C_{kl}} \frac{\partial C_{kl}}{\partial t} \quad (\text{S10})$$

where the last term changes sign from erosion to clogging, i.e.,  $\partial C_{kl}/\partial t = \pm \alpha \pi q_{kl}^m / r_{kl}^{n-3} \mu l_{kl}$  for erosion and clogging respectively. As a result, the magnitude of change in the order parameter equals that of erosion. Note that in Eq.

(S10), the second term depends on the network topology, and pore throat clogging results in the change of network topology at later times. At short times, however, similar to the erosion, a phase transition exists at  $n = 3$ . When  $n < 3$  the network moves toward homogenization during the clogging process and when  $n > 3$  the flow moves toward the development of channeling instability. At later times, this initial trend, however, might not hold true due to the aforementioned complex changes in the connectivity network during the clogging process.

## S7. GENERAL SHEAR DEPENDENT EROSION MODEL

As an example of a nonlinear erosion model, we consider a shear-dependent erosion

$$\frac{dr}{dt} = f(\tau), \quad (\text{S11})$$

where  $\tau = \tau(q, r) = 4\mu q/\pi r^3$  is the shear stress at the tube's wall assuming Poiseuille flow. It is to be noted that a shear-dependent erosion model is commonly used in studying erosion [6–8] wherein such models erosion happens linearly proportional to the shear stress at the wall only after a certain threshold value  $\tau_0$  (see main text for more information). Such linear models, however, ignore the maximum detachment rate of particles at the pore's boundary which would effectively limit the pore's radius maximum rate of change. To address this, we use a nonlinear erosion model

$$f(\tau) = \alpha (\tanh [\beta(\tau - \tau_0)] + 1), \quad (\text{S12})$$

where  $\beta$  determines the shear rate scale and  $\alpha$  determines the erosion rate scale. Note that the erosion rate scale  $\alpha$  only affects the timescale at which the final state is reached and has no effect on the pattern formation. Without loss of generality we set  $\alpha = 1$ . Following the local dynamics model discussion in the main text, one can find that the homogenization condition reduces to

$$f(\tau) > \tau \frac{df(\tau)}{d\tau}. \quad (\text{S13})$$

Assuming a random network (Fig. S8a), the initial values of shear stress at the walls have a decaying distribution over a large set of values (Fig. S8b). To test our local dynamics model, we vary  $\beta$  and  $\tau_0$  and run three different tests: (i)  $\beta = 1, \tau_0 = 1$ : For such values of  $\beta, \tau$ , almost all the tubes are in the homogenization region corresponding to Eq. (S13) (Fig. S8c) and the network moves toward homogenization (Fig. S8d). The final PDF of the network after erosion is further shown in (Fig. S8e). (ii)  $\beta = 1, \tau_0 = 12$ : In this case, the homogenization condition is satisfied at some finite value of shear stress  $\tau_0$  where  $f(\tau_0) = \tau_0 f'(\tau_0)$ . As a result, some edges would homogenize, and some would channelize (Fig. S8f). Running the simulation over a random network, we find that a finite number of channels form (Fig. S8g). The PDF distribution of shear stress at the wall  $\tau$  correspondingly becomes bimodal (Fig. S8h). (iii)  $\beta = 1, \tau_0 = 30$ : In this case, almost all the edges in the network are in the channelization regime (Fig. S8i), and performing the simulations we find that indeed one strong single channel is formed (Fig. S8j) and the PDF of shear stress  $\tau$  shows a clear separation between flow in the channel versus flow in the rest of the system (Fig. S8k).

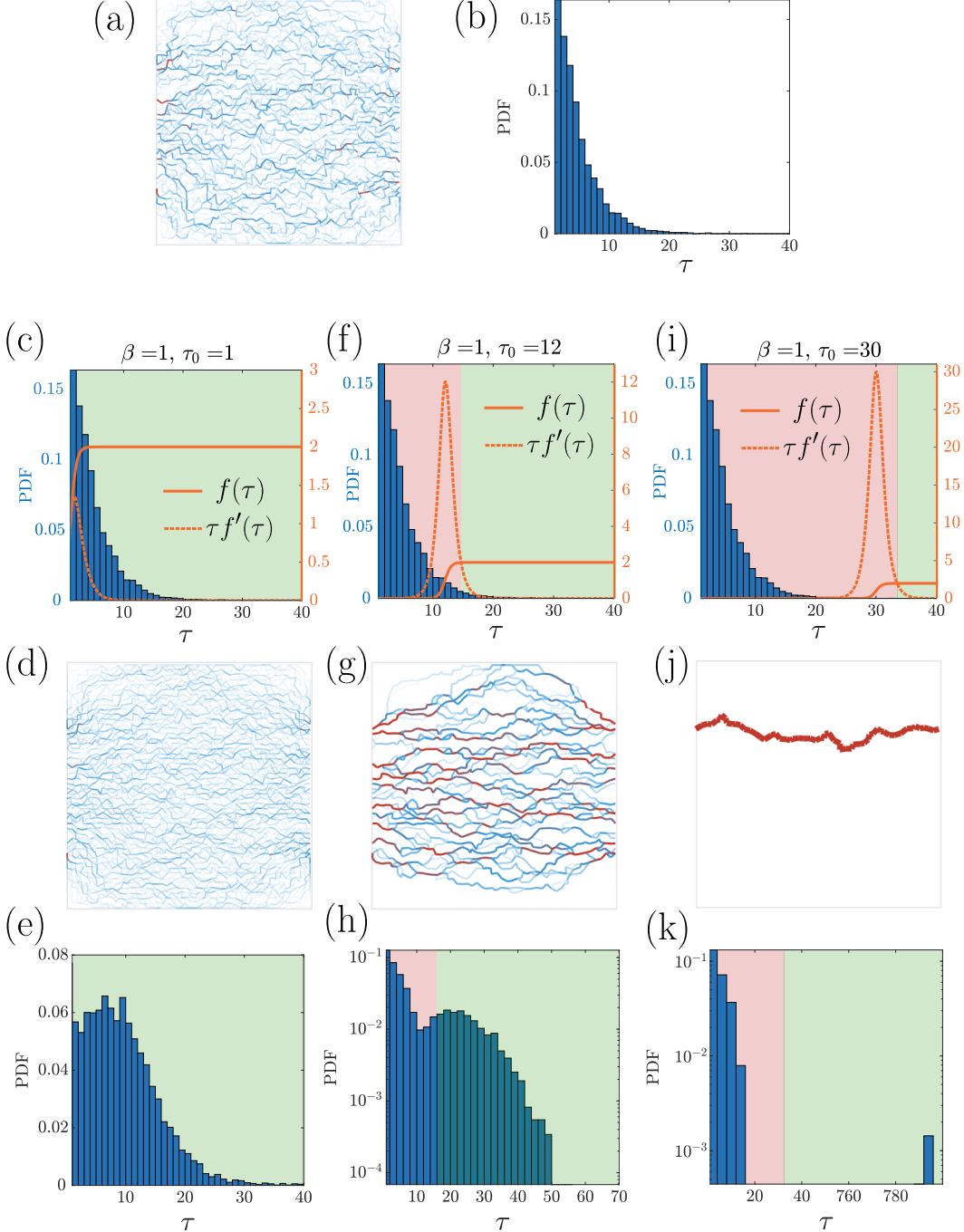


FIG. S8: (a) A 2D random network with  $N_x = 50$  and  $N_y = 50$  points. (b) The probability distribution function (PDF) of the shear stress for the edges of the network. (c)/(f)/(i) The PDF of the shear stress along with nonlinear erosion law  $f(\tau)$  (solid red line) and  $\tau f'(\tau)$  (dashed red line). The areas where the homogenization condition (i.e.,  $f(\tau) > \tau f'(\tau)$ ) is satisfied are shaded with green color, otherwise, the channelization condition is satisfied and the region is shaded with red color. (d)/(g)/(j) Snapshots of the 2D network after erosion using the nonlinear erosion law shown in the previous row until the average radius of the network is increased to twice its original size. (e)/(h)/(k) The PDF of the shear stress at the walls for the final snapshot of the network shown in the previous row.

The PDF of the shear stress at the walls for the final snapshot of the network shown in the previous row.

- 
- [1] Network instability, <https://github.com/ahmadzareei/networkInstability> (2021).
  - [2] C.-h. Liu, S. R. Nagel, D. Schecter, S. Coppersmith, S. Majumdar, O. Narayan, and T. Witten, Force fluctuations in bead packs, *Science* **269**, 513 (1995).
  - [3] S. Coppersmith, C.-h. Liu, S. Majumdar, O. Narayan, and T. Witten, Model for force fluctuations in bead packs, *Physical Review E* **53**, 4673 (1996).
  - [4] K. Alim, S. Parsa, D. A. Weitz, and M. P. Brenner, Local pore size correlations determine flow distributions in porous media, *Physical Review Letters* **119**, 144501 (2017).
  - [5] S. Parsa, A. Zareei, E. Santanach-Carreras, E. J. Morris, A. Amir, L. Xiao, and D. A. Weitz, Unexpected scaling of interstitial velocities with permeability due to polymer retention in porous media, *Physical Review Fluids* **6**, L082302 (2021).
  - [6] R. Jäger, M. Mendoza, and H. J. Herrmann, Channelization in porous media driven by erosion and deposition, *Physical Review E* **95**, 013110 (2017).
  - [7] S. Bonelli and D. Marot, Micromechanical modeling of internal erosion, *European Journal of Environmental and Civil Engineering* **15**, 1207 (2011).
  - [8] G. Parker and N. Izumi, Purely erosional cyclic and solitary steps created by flow over a cohesive bed, *Journal of Fluid Mechanics* **419**, 203 (2000).